Additional file 1 for

InSAR constraints on spatiotemporal changes in plate coupling beneath Shikoku along the Nankai subduction zone

K. Shimotsuma[1,2], Y. Kinoshita[3], S. Yabe[2], and T. Ochi[2]

[1] Graduate School of Systems and Information Engineering, University of Tsukuba.

[2] Geological Survey of Japan, National Institute of Advanced Industrial Science and Technology.

[3] Institute of Systems and Information Engineering, University of Tsukuba.

Contents of this file

Text S1 to S3

Figures S1 to S15

Tables S1 to S2

Text S1. GNSS processing

Original GNSS coordinates contain tectonic effects not related to plate coupling along the Nankai subduction zone, so we first corrected them. One of these effects which we need to correct is the postseismic deformation of the 2011 Tohoku-oki earthquake. Because the magnitude of the 2011 Tohoku-oki earthquake was so large (M_w 9.0), the earthquake affected trends of GNSS coordinates even in western Japan after the mainshock: 11 March 2011. We corrected the postseismic deformation from GEONET and GNSS-A coordinates using a logarithmic function fitting approach based on Tobita (2016). We first fitted the following function (S1) to the GNSS daily coordinates of the kth component (eastward, northward or upward) at the lth station:

$$X_{k,l}(t) = a_{k,l} + b_{k,l}\,t + c_{k,l}\,cos(2\pi t) + d_{k,l}\,sin(2\pi t) + e_{k,l}\,cos(4\pi t) + f_{k,l}\,sin(4\pi t)$$
$$+ \sum_n g_{k,l,n}\,H(t - T_n) + h_{k,l}\,log\left(1 + \frac{t - T_{3.11}}{4.025 \times 10^{-3}}\right) + i_{k,l}\,log\left(1 + \frac{t - T_{3.11}}{3.376 \times 10^{-1}}\right), \quad \text{(S1)}$$

where $X_{k,l}$ indicates the modeled displacement as a function of time t. The coefficients on the right-hand side $a_{k,l}$ through $i_{k,l}$ are unknown parameters to be estimated via the least-squares method, H is the Heaviside step function, and T denotes the date of events specified below. The linear term on the right-hand side represents a linear trend (i.e., velocity). We assumed that it reflected the sum of the Amur plate (AM) rigid rotation and the plate coupling along the Nankai subduction zone. The trigonometric terms explain annual and semiannual variations, which are assumed to be temporally constant. The seventh term explains offsets caused by station maintenance, where T_n indicates the time when the nth maintenance was conducted. We referred to the station maintenance information on the GSI homepage to determine T_n. The two logarithmic terms explain the postseismic displacements of the 2011 Tohoku-oki earthquake. $T_{3.11}$ indicates the time of

the mainshock of the 2011 Tohoku-oki earthquake, whereas 4.025×10^{-3} and 3.376×10^{-1} correspond to relaxation times [years] obtained via the nonlinear least-squares method performed by Tobita (2016). Indeed, Tobita (2016) suggested that the postseismic deformation can be modeled by a linear combination of the two logarithmic terms and an exponential term, $exp\left(-\frac{t-T_{3.11}}{1232}\right)$. However, the long relaxation time of the exponential term (1232 years) makes the evolution of the exponential term similar to that of the linear term. Thus, we omitted the exponential term as Shimotsuma et al. (2026) did. We conducted the function fitting for the 577 GEONET stations within longitudes 130°E to 139°E and latitudes 31°N to 36°N using coordinates from 12 March 2011 to 31 December 2013. There were no earthquakes which produced significant coseismic displacements in this period. We did not use GNSS-A data in the function fitting, because the sparse temporal resolution of GNSS-A coordinates made it difficult to estimate $h_{k,l}$ and $i_{k,l}$ robustly. Considering the distance from the epicenter, postseismic displacements of the 2011 Tohoku-oki earthquake should be spatially smooth in western Japan. We spatially smoothed distributions of estimated $h_{k,l}$ and $i_{k,l}$ by approximating them by quadratic polynomials. Note that we removed outliers, Kouchisaga-A (081172) and Sekigahara (970812), by visual inspection before estimating the quadratic planes. Using spatially smoothed $h_{k,l}$ and $i_{k,l}$, we corrected the postseismic displacement of the 2011 Tohoku-oki earthquake from GNSS original coordinates.

We also corrected coseismic displacements of three earthquakes: the 2016 Kumamoto (M_w7.0), 2024 Noto (M_w7.5), and 2024 Hyuga-nada (M_w7.0) earthquakes. We calculated these coseismic displacements using published fault models (GSI 2024; Suito et al. 2024; Yarai et al. 2016) and subtracted them from GNSS coordinates.

After correcting the postseismic and coseismic displacements described above, we estimated velocities in each period. We re-conducted function fitting, but we fitted another function:

$$X_{k,l}(t) = a_{k,l} + \sum_{m=1,2,3} b_{k,l,m}(t-\tau_m)H(t-\tau_m) + c_{k,l}\,cos(2\pi t) + d_{k,l}\,sin(2\pi t)$$
$$+e_{k,l}\,cos(4\pi t) + f_{k,l}\,sin(4\pi t) + \sum_{n} g_{k,l,n}\,H(t-T_n) \quad \text{(S2)}$$

to the corrected GNSS coordinates, where τ_1, τ_2, and τ_3 indicate the first date of period (i), (ii), and (iii), respectively: 1 September 2014, 1 October 2018, and 1 September 2019. Compared with the equation (S1), we removed logarithmic terms because we already corrected the postseismic displacements. We also modified the second term by introducing a piecewise linear term. Thus, velocities during periods (i), (ii), and (iii) can be written as $b_{k,l,1}$, $b_{k,l,1} + b_{k,l,2}$, and $b_{k,l,1} + b_{k,l,2} + b_{k,l,3}$, respectively.

Finally, we projected GNSS velocities into an upper plate reference frame using an AM absolute rotation model (DeMets et al. 2010).

Text S2. InSAR processing

We first concatenated adjacent frames acquired with the same path and off-nadir angle. Then, we made interferograms for all possible interferometric pairs in each concatenated frame. Interferograms were spatially averaged by multilook processing, which increased the pixel spacing to approximately 100 m in both the range and azimuth directions to improve the signal-to-noise ratio. Orbital and topographic fringes were corrected using ALOS-2 precise orbit information and the 30 m resolution digital elevation model of the Shuttle Radar Topography Mission (Farr et al. 2007). We applied a spectral filter (Goldstein and Werner 1998), and we then performed two-dimensional phase unwrapping based on the minimum-flow algorithm (Costantini 1998).

We then corrected phase changes caused by atmospheric, solid earth tide, and earthquake effects to extract signals related to plate coupling along the Nankai subduction zone. Interferograms made from L-band SAR data contain ionospheric phase advances. We corrected the ionospheric phase advance by the split spectrum method (SSM; Wegmüller et al. 2018). The SSM estimates ionosphere-originated phase change utilizing its dispersive nature. The dispersive component of the phase change $\Delta\phi_{dispersive}$ can be written as

$$\Delta\phi_{dispersive} = x\Delta\phi_0 + z(\Delta\phi_H - \Delta\phi_L) \tag{S3}$$

with

$$x = \frac{f_H\ f_L}{f_0^2 + f_H\ f_L}, \tag{S4}$$

$$z = -\frac{f_0\ f_H\ f_L}{(f_0^2 + f_H\ f_L)(f_H\ - f_L\ )}. \tag{S5}$$

Here, $\Delta\phi_0$ indicates an interferogram of the full bandwidth with a center frequency f_0, whereas $\Delta\phi_H$ and $\Delta\phi_L$ indicate interferograms of higher- and lower-frequency subbands with center frequencies f_H, f_L. In this study, we split the range frequency band into three equally spaced parts and used higher-frequency and lower-frequency bands to generate $\Delta\phi_H$ and $\Delta\phi_L$. We then spatially filtered the $\Delta\phi_{dispersive}$ based on the method of Nagaoka et al. (2025) under the assumption that the ionospheric phase variation is spatially smooth. We regarded the filtered dispersive phase change as the ionospheric noise.

We corrected phase changes due to neutral atmospheric delay based on Kinoshita (2022). We estimated the slant path delay (SPD) at each SAR observation time from zenith total delay (ZTD) and its horizontal gradient observed by GNSS. We used 5-minute GNSS atmospheric products provided by the Nevada Geodetic Laboratory at the University of Nevada. For each pair, we converted the difference of the SPD between the primary and secondary SAR observations into a phase change and subtracted it from the interferogram.

Solid Earth tide can produce spatial phase variations on the order of millimeters to centimeters within a SAR frame (Yunjun et al. 2022). Thus, we also corrected phase changes due to solid earth tide using the PySolid Python module developed by Yunjun et al. (2022) and Milbert (2018).

As with the case of GNSS data, interferograms contain postseismic displacements of the 2011 Tohoku-oki earthquake and coseismic displacements of other great earthquakes. We calculated postseismic displacements of the 2011 Tohoku-oki earthquake for each interferometric pair using spatially interpolated $h_{k,l}$ and $i_{k,l}$ in equation (S1). We then projected the interpolated postseismic displacements into line-of-sight (LOS) directions and subtracted them from interferograms. We corrected coseismic phase changes

associated with the three earthquakes using fault models (GSI 2024; Suito et al. 2024; Yarai et al. 2016) as we did for GNSS data.

After generating interferograms with corrections described above, we conducted a small baseline subset (SBAS)-based time series analysis (Berardino et al. 2002). For each pixel, we estimated incremental phase changes from observed phase changes. We can write an observed phase change generated from SAR images acquired on ith and jth observation dates $\Delta\phi_{i,j}$ as

$$\Delta\phi_{i,j} = \sum_{k=i}^{j-1} \phi_{k,k+1} + \delta_{i,j}, \tag{S6}$$

where $\phi_{k,k+1}$ indicates the unknown incremental phase change between kth and $(k+1)$th SAR observation dates, and $\delta_{i,j}$ is the error contained in the observed phase change $\Delta\phi_{i,j}$. We can express equation (S6) in a matrix form:

$$\boldsymbol{\Delta\phi} = \boldsymbol{H\phi} + \boldsymbol{\delta}, \tag{S7}$$

where $\boldsymbol{\Delta\phi}$ and $\boldsymbol{\delta}$ contain observed phase changes and corresponding errors, respectively. $\boldsymbol{\phi}$ contains unknown $M-1$ incremental phase changes as $\boldsymbol{\phi} = \left[\phi_{1,2}, \phi_{2,3}, \dots, \phi_{M-1,M}\right]^{\boldsymbol{T}}$, where M indicates the number of SAR images. We estimated $\boldsymbol{\phi}$ via the least-squares method assuming $\boldsymbol{\delta}$ follows a Gaussian distribution with zero mean. We removed unreliable interferograms that contained artifact or severe noise via visual inspection before conducting the time series analysis. Except for the removed interferograms, we used all available interferometric pairs including long temporal pairs. The signal-to-noise ratio of long temporal pairs is higher than that of short temporal pairs although long temporal pairs tended to have low coherence.

Using estimated incremental phase changes $\boldsymbol{\phi}$, we calculated cumulative displacements. Then, we estimated velocity in each period by the function fitting as we did in the GNSS processing. However, unlike the GNSS analysis, we did not estimate annual and semiannual changes for InSAR because the number of SAR images was insufficient to estimate them robustly.

GNSS and InSAR velocities should have the same reference frame. For each frame, we first removed the AM rigid rotation effect from the InSAR velocity fields. Then, we added a spatially uniform offset that minimized root mean square error (RMSE) between GNSS velocities projected to the LOS directions and corresponding InSAR velocities.

Text S3. Kinematic fault slip inversion

We express the relationship between observed data and unknown model parameters as

$$\boldsymbol{d_{GNSS}} = \left[\boldsymbol{G_s^{GNSS}}\ \boldsymbol{G_{off}^{GNSS}}\right]\begin{bmatrix}\boldsymbol{s}\\ \boldsymbol{v_{off}^{GNSS}}\end{bmatrix} + \boldsymbol{e_{GNSS}}, \tag{S8}$$

$$\boldsymbol{d_{SAR}} = \left[\boldsymbol{G_s^{SAR}}\ \ \boldsymbol{G_{off}^{SAR}}\right]\begin{bmatrix}\boldsymbol{s}\\ \boldsymbol{v_{off}^{SAR}}\end{bmatrix} + \boldsymbol{e_{SAR}}. \tag{S9}$$

Here, $\boldsymbol{d}$ is the data vector, $\boldsymbol{s}$ and $\boldsymbol{v_{off}}$ contain unknown model parameters (slip deficit rates and velocity offsets between data and model), $\boldsymbol{G_s}$ and $\boldsymbol{G_{off}}$ explain the relationship between the data and model parameters, and $\boldsymbol{e}$ is the error vector. Data vectors $\boldsymbol{d_{GNSS}}$ and $\boldsymbol{d_{SAR}}$ contain GNSS and InSAR velocities, respectively. In the inversions, we used eastward, northward, and upward velocities of 107 GEONET and 10 GNSS-A stations around Shikoku (Figure S1). As shown in Figure S1, we excluded four GEONET stations (021042, 041132, 950436, and 960652) and a GNSS-A station (MRT3) because they probably contained large uncertainties or non-tectonic effects. We used InSAR velocities in 1,222 pixels from descending frames and 1,121 pixels from ascending frames, which were chosen by a spatially uniform downsampling with a 3.8 × 3.8 km window to reduce the computational cost. The unknown model parameters are slip deficit rate on each subfault $\boldsymbol{s}$, with the slip direction fixed parallel to the Amur plate (AM)-Philippine Sea plate (PH) convergence direction, and velocity offsets between data and model $\boldsymbol{v_{off}}$. We distributed 406 triangular subfaults on the plate interface at depths of 0–40 km (Figure S1). We chose this depth range because stable sliding may take place downdip of the low-frequency earthquakes (LFEs) (Yoshioka and Murakami 2007), and most LFEs occur at depths shallower than 40 km in the Nankai region (Figure 1b). Side length of each

triangular subfault was about 25 km. We introduced velocity offsets separately for eastward, northward, and upward components of the GEONET data, for eastward, northward, and upward components of the GNSS-A data, and for LOS components of the six concatenated SAR frames. $\boldsymbol{G_s}$ explains the relationship between surface velocities and fault slips in a homogeneous elastic half-space (Lindsey 2024; Nikkhoo and Walter 2015). $\boldsymbol{G_{off}}$ maps the velocity offsets to the corresponding GNSS and InSAR data. Each row of $\boldsymbol{G_{off}}$ contains a value of 1 in the column corresponding to the offset parameter and 0 elsewhere. Error vectors $\boldsymbol{e_{GNSS}}$ and $\boldsymbol{e_{SAR}}$ contain both observation and modeling errors. We assumed that they follow Gaussian distributions with zero means and covariances of $\sigma_{GNSS}^2\boldsymbol{E_{GNSS}}$ and $\sigma_{SAR}^2\boldsymbol{E_{SAR}}$:

$$\boldsymbol{e_{GNSS}} \sim \boldsymbol{N}(\boldsymbol{0}, \sigma_{GNSS}^2\boldsymbol{E_{GNSS}}), \tag{S10}$$

$$\boldsymbol{e_{SAR}} \sim \boldsymbol{N}(\boldsymbol{0}, \sigma_{SAR}^2\boldsymbol{E_{SAR}}), \tag{S11}$$

where σ_{GNSS}^2 and σ_{SAR}^2 indicate unknown scale factors for GNSS and SAR data covariance matrices, respectively. We used the squared standard errors of the estimated GNSS velocities obtained in the GNSS processing for the diagonal components of $\boldsymbol{E_{GNSS}}$ while we assumed zero for non-diagonal components. We expressed $\boldsymbol{E_{SAR}}$ as

$$\boldsymbol{E_{SAR}} = \begin{bmatrix} \boldsymbol{E^{Des-WS}} & & & & & \\ & \boldsymbol{E^{Des-CS}} & & & & \\ & & \boldsymbol{E^{Des-ES}} & & & \\ & & & \boldsymbol{E^{Asc-WS}} & & \\ & & & & \boldsymbol{E^{Asc-CS}} & \\ & & & & & \boldsymbol{E^{Asc-ES}} \end{bmatrix} \tag{S12}$$

where each subscript indicates the frame names. We defined the ij component of each matrix as

$$\left[\boldsymbol{E^{Des-WS}}\right]_{\boldsymbol{ij}} = \exp\left(-\frac{r_{ij}}{10000}\right), \tag{S13}$$

where r_{ij} indicates the distance [m] between pixels i and j (Fukahata and Wright 2008). We assumed there were no correlations among velocities from different frames.

We combined equations (S8) and (S9) into an observation equation in the joint inversion:

$$\boldsymbol{d} = \boldsymbol{G}\boldsymbol{m} + \boldsymbol{e} \tag{S14}$$

with

$$\boldsymbol{d} = \begin{bmatrix} \boldsymbol{d_{GNSS}} \\ \boldsymbol{d_{SAR}} \end{bmatrix}, \tag{S15}$$

$$\boldsymbol{G} = \begin{bmatrix} \boldsymbol{G_s^{GNSS}} & \boldsymbol{G_{off}^{GNSS}} & \boldsymbol{0} \\ \boldsymbol{G_s^{SAR}} & \boldsymbol{0} & \boldsymbol{G_{off}^{SAR}} \end{bmatrix}, \tag{S16}$$

$$\boldsymbol{m} = \begin{bmatrix} \boldsymbol{s} \\ \boldsymbol{v_{off}^{GNSS}} \\ \boldsymbol{v_{off}^{SAR}} \end{bmatrix}, \tag{S17}$$

$$\boldsymbol{e} = \begin{bmatrix} \boldsymbol{e_{GNSS}} \\ \boldsymbol{e_{SAR}} \end{bmatrix}. \tag{S18}$$

We expressed the covariance matrix of the combined data as $\sigma_{GNSS}^2 \boldsymbol{E}(\alpha^2)$, where

$$\boldsymbol{E}(\alpha^2) = \begin{bmatrix} \boldsymbol{E_{GNSS}} & \boldsymbol{0} \\ \boldsymbol{0} & \alpha^2 \boldsymbol{E_{SAR}} \end{bmatrix} \tag{S19}$$

by assuming no correlation between GNSS and InSAR data and introducing a hyperparameter $\alpha^2 = \frac{\sigma_{SAR}^2}{\sigma_{GNSS}^2}$, which indicates the relative variance of the GNSS-InSAR data sets.

We introduced prior information: slip deficit distribution is spatially smooth to some extent. We expressed the smoothing constraint as

$$\frac{2}{\sum_{j=1}^{3} l_{ij}} \sum_{j=1}^{3} \frac{s_j - s_i}{l_{ij}} - \varepsilon_i = 0 \tag{S20}$$

(Maerten et al. 2005), where s_i indicates the slip (deficit) rate on the ith subfault, s_j indicates slip deficit rates on adjacent subfaults, l_{ij} indicates the distance between ith and jth subfaults, and ε_i indicates the uncertainty of the smoothing constraint. We can express this smoothing constraint in a matrix form:

$$\mathbf{0} = \boldsymbol{Lm} + \boldsymbol{\varepsilon}, \tag{S21}$$

where $\boldsymbol{L}$ represents a smoothing matrix. We expressed the uncertainty of the prior information as $\boldsymbol{\varepsilon}$ assuming $\boldsymbol{\varepsilon} \sim N(\mathbf{0}, \rho^2 \boldsymbol{E_L})$, where ρ^2 is an unknown scaling factor, and $\boldsymbol{E_L}$ is determined based on a method of Ader et al. (2012):

$$\boldsymbol{E_L} = \begin{bmatrix} \frac{1}{w_1^2} & & \\ & \ddots & \\ & & \frac{1}{w_M^2} \end{bmatrix}. \tag{S22}$$

Here, M indicates the length of $\boldsymbol{m}$. w_i^2 minimizes $\sum_{j=1}^{M} \left(\frac{[\boldsymbol{R_m}]_{ji}}{[\boldsymbol{R_m}]_{ii}} - e^{-\frac{l_{ij}^2}{2w_i^2}} \right)^2$ where $\boldsymbol{R_m}$ is a resolution matrix of the model parameters given as

$$\boldsymbol{R_m} = \left(\boldsymbol{G^T E} (\alpha^2)^{-1} \boldsymbol{G} + \beta^2 \boldsymbol{L^T E_L^{-1} L} \right)^{-1} \boldsymbol{G^T E} (\alpha^2)^{-1} \boldsymbol{G}. \tag{S23}$$

β^2 is a hyperparameter given by $\beta^2 = \frac{\sigma_{GNSS}^2}{\rho^2}$, which explains the relative weight of the slip smoothness to the GNSS data. Introducing the method of Ader et al. (2012) allows well-resolved subfaults to have small smoothness, whereas poorly resolved subfaults are strongly smoothed (Thomas et al. 2014).

Now, the kinematic fault slip inversion analysis is summarized by minimizing the cost function $f(\boldsymbol{m}; \alpha^2, \beta^2)$:

$$f(\boldsymbol{m}; \alpha^2, \beta^2) = (\boldsymbol{d} - \boldsymbol{Gm})^T \boldsymbol{E} (\alpha^2)^{-1} (\boldsymbol{d} - \boldsymbol{Gm}) + \beta^2 (\boldsymbol{Lm})^T \boldsymbol{E_L^{-1}} (\boldsymbol{Lm}), \tag{S24}$$

When α^2, β^2 are given, the least-squares solution $\widehat{\boldsymbol{m}}$, which minimizes $f(\boldsymbol{m}; \alpha^2, \beta^2)$, is

$$\widehat{\boldsymbol{m}}(\alpha^2, \beta^2) = \left(\boldsymbol{G^T E}(\alpha^2)^{-1}\boldsymbol{G} + \beta^2 \boldsymbol{L^T E_L^{-1} L}\right)^{-1} \boldsymbol{G^T E}(\alpha^2)^{-1}\boldsymbol{d}\,. \quad \text{(S25)}$$

We determined the optimal hyperparameters $\hat{\alpha}^2$ and $\hat{\beta}^2$ by minimizing the Akaike Bayesian information criterion (ABIC) (Funning et al. 2014). The stochastic relationship between observed data and model parameters is

$$p(\boldsymbol{d}|\boldsymbol{m};\ \sigma_{GNSS}^2, \alpha^2) = (2\pi\sigma_{GNSS}^2)^{-\frac{N}{2}} |\boldsymbol{E}(\alpha^2)|^{-\frac{1}{2}} exp\left(-\frac{1}{2\sigma_{GNSS}^2}(\boldsymbol{d}-\boldsymbol{Gm})^T \boldsymbol{E}(\alpha^2)^{-1}(\boldsymbol{d}-\boldsymbol{Gm})\right). \text{(S26)}$$

Here, N indicates the length of $\boldsymbol{d}$. We can also express the prior information (i.e. the smoothing constraint) as a probability density function:

$$p(\boldsymbol{m}; \rho^2) = (2\pi\rho^2)^{-\frac{L_r}{2}} |\Lambda_L|^{\frac{1}{2}} exp\left(-\frac{1}{2\rho^2}(\boldsymbol{Lm})^T \boldsymbol{E_L^{-1}}(\boldsymbol{Lm})\right) \quad \text{(S27)}$$

where L_r is the rank of $\boldsymbol{L^T E_L^{-1} L}$ and $|\Lambda_L|$ is the absolute value of the product of non-zero eigenvalues for $\boldsymbol{L^T E_L^{-1} L}$. We calculated the posterior probability using Bayes' theorem as

$$p(\boldsymbol{m}; \sigma_{GNSS}^2, \alpha^2, \beta^2|\boldsymbol{d}) = c(2\pi\sigma_{GNSS}^2)^{-\frac{N}{2}} \left(2\pi(\frac{\sigma_{GNSS}}{\beta})^2\right)^{-\frac{L_r}{2}} |\boldsymbol{E}(\alpha^2)|^{-\frac{1}{2}} |\Lambda_L|^{\frac{1}{2}} \exp\left(-\frac{1}{2\sigma_{GNSS}^2} f(\boldsymbol{m}; \alpha^2, \beta^2)\right) \text{(S28)}$$

Here, c is a normalizing factor independent of model parameters and hyperparameters. In this case, we can calculate the marginal likelihood $\mathcal{L}(\sigma_{GNSS}^2, \alpha^2, \beta^2|\boldsymbol{d})$ by integrating $p(\boldsymbol{m}; \sigma_{GNSS}^2, \alpha^2, \beta^2|\boldsymbol{d})$ as

$$\begin{aligned}\mathcal{L}(\sigma_{GNSS}^2, \alpha^2, \beta^2|\boldsymbol{d}) &= \int p(\boldsymbol{m}; \sigma_{GNSS}^2, \alpha^2, \beta^2|\boldsymbol{d})\, d\boldsymbol{m} \\ &= c(2\pi\sigma_{GNSS}^2)^{-\frac{N+L_r-M}{2}} (2\pi\beta^2)^{\frac{L_r}{2}} \left|\boldsymbol{G^T E}(\alpha^2)^{-1}\boldsymbol{G}\right. \\ &\left. + \beta^2 \boldsymbol{L^T E_L^{-1} L}\right|^{-\frac{1}{2}} |\Lambda_L|^{\frac{1}{2}} |\boldsymbol{E}(\alpha^2)|^{-\frac{1}{2}} \exp\left(-\frac{1}{2\sigma_{GNSS}^2} f(\widehat{\boldsymbol{m}}; \alpha^2, \beta^2)\right) \quad \text{(S29)}\end{aligned}$$

Using the definition of ABIC, $ABIC = -2\log(\mathcal{L})$, we obtained

$$ABIC(\alpha^2, \beta^2) = (N + L_r - M)\, log\big(f(\widehat{\boldsymbol{m}}; \alpha^2, \beta^2)\big) - L_r\, log(\beta^2) + log\left|\boldsymbol{G^T E}(\alpha^2)^{-1}\boldsymbol{G} + \beta^2 \boldsymbol{L^T E_L^{-1} L}\right| + log|\boldsymbol{E}(\alpha^2)| + const. \quad (S30)$$

We searched for $\hat{\alpha}^2$and $\hat{\beta}^2$ which minimize the ABIC, and then we obtained corresponding $\widehat{\boldsymbol{m}}$ by substituting the $\hat{\alpha}^2$ and $\hat{\beta}^2$ into equation (S25). We can analytically calculate $\hat{\sigma}^2_{GNSS}$, which maximizes $\mathcal{L}$, when $\hat{\alpha}^2$ and $\hat{\beta}^2$ are given:

$$\hat{\sigma}^2_{GNSS} = \frac{f\big(\widehat{\boldsymbol{m}}; \hat{\alpha}^2, \hat{\beta}^2\big)}{N + L_r - M}. \quad (S31)$$

We can also obtain the posterior covariance matrix of the model parameters:

$$\boldsymbol{E_m} = \hat{\sigma}^2_{GNSS}\big(\boldsymbol{G^T E}(\hat{\alpha}^2)^{-1}\boldsymbol{G} + \hat{\beta}^2 \boldsymbol{L^T E_L^{-1} L}\big)^{-1}. \quad (S32)$$

Note that we estimate $\boldsymbol{E_L}$ in addition to the hyperparameters as explained above. Because the values of $\boldsymbol{E_L}$ and hyperparameters affect each other, we estimated them by following procedure. First, we estimated hyperparameters assuming that $\boldsymbol{E_L} = \boldsymbol{I}$, where $\boldsymbol{I}$ is an identity matrix. Next, we calculated $\boldsymbol{R_m}$ using equation (S23). Then, we can obtain a new $\boldsymbol{E_L}$ and corresponding hyperparameters. We iterated this procedure until the values of $\boldsymbol{E_L}$ and hyperparameters converged.

References cited in Supplementary Information

Fukahata Y, Wright TJ (2008) A non-linear geodetic data inversion using ABIC for slip distribution on a fault with an unknown dip angle. Geophys J Int 173(2):353–364. doi:10.1111/j.1365-246X.2007.03713.x

Nagaoka S, Takada Y, Morishita Y (2025) Improved application of the split-spectrum method to L-band interferograms for ionospheric phase mitigation: a practical recipe. Earth Planets Space 77:82. doi:10.1186/s40623-025-02206-9

Thomas MY, Avouac JP, Champenois J, Lee JC, Kuo LC (2014) Spatiotemporal evolution of seismic and aseismic slip on the Longitudinal Valley Fault, Taiwan. J Geophys Res Solid Earth 119:5114–5139. doi:10.1002/2013JB010603

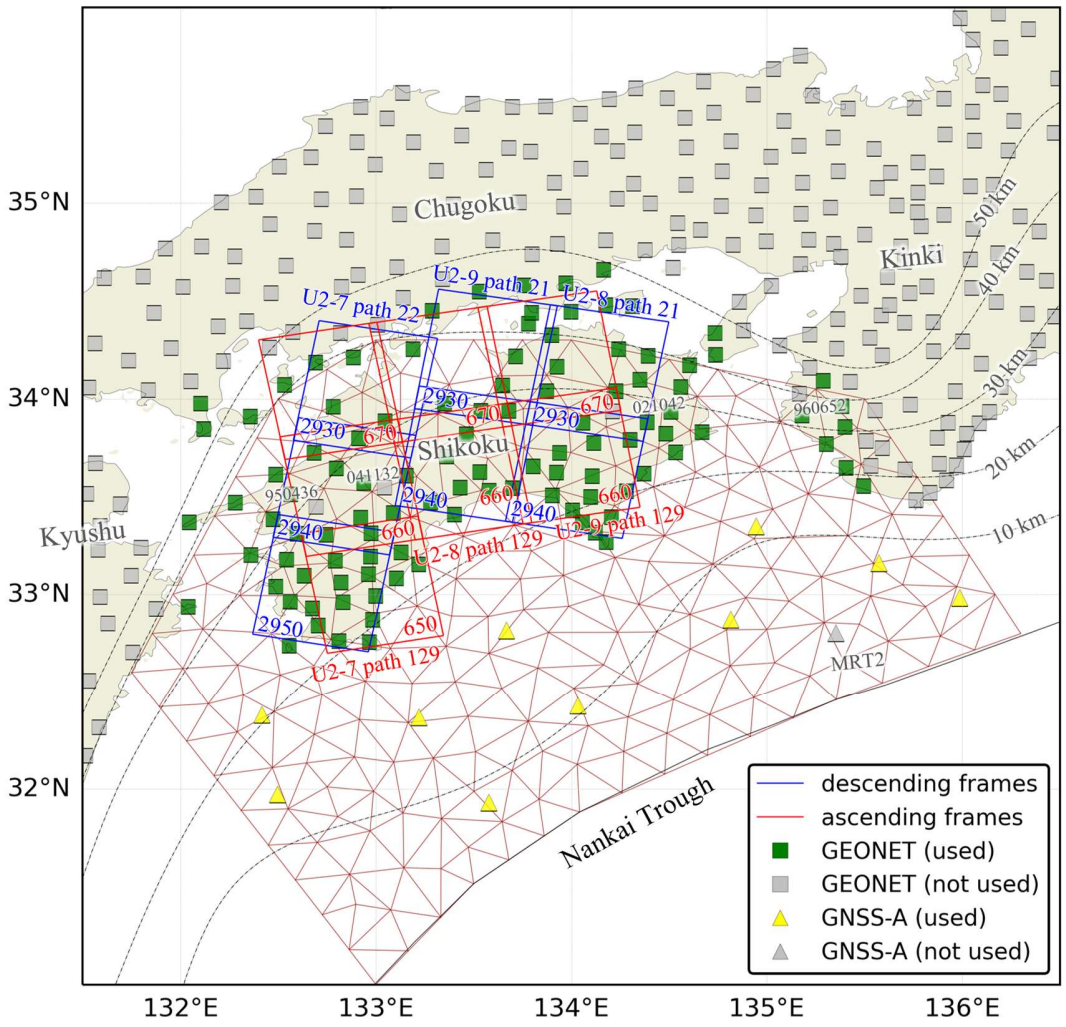


Figure S1. Velocity data and subfault distribution used in the kinematic fault slip inversion. Blue and red rectangles indicate ALOS-2 descending and ascending frames, respectively. Green squares indicate GEONET, and yellow triangles indicate GNSS-A stations used in the inversion. Gray squares and triangles indicate stations not used in the inversion. Subfaults along the Nankai subduction zone are indicated as brown triangles.

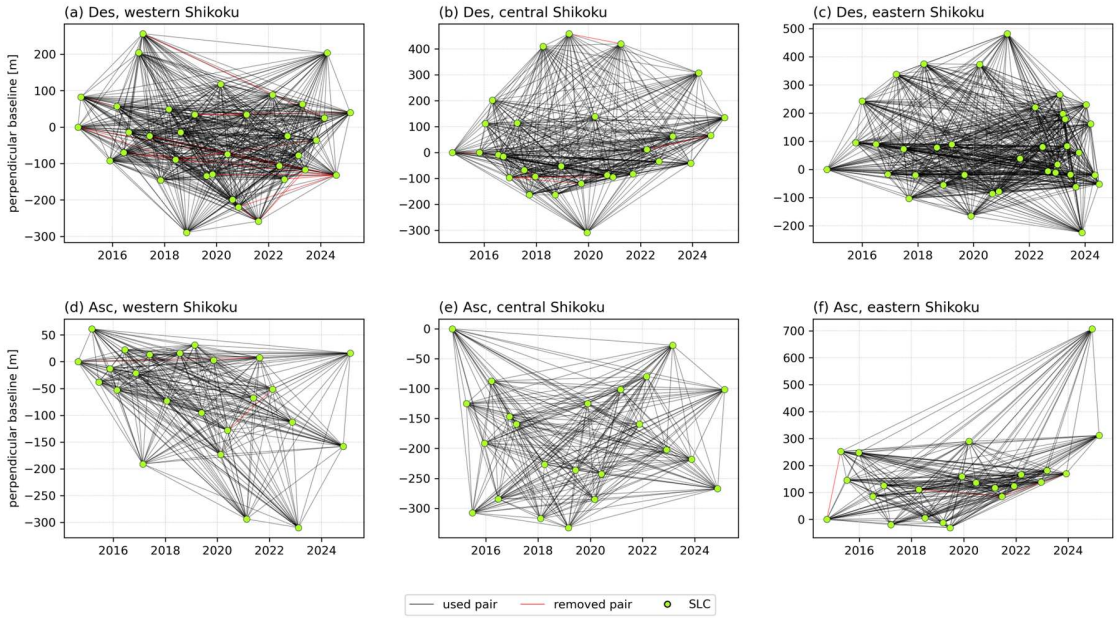


Figure S2. Interferometric networks used in the InSAR time-series analysis. ALOS-2 data acquisition dates are indicated as light-green circles. Black lines indicate interferometric pairs used for the time series analysis, whereas red lines indicate pairs removed by visual inspection.

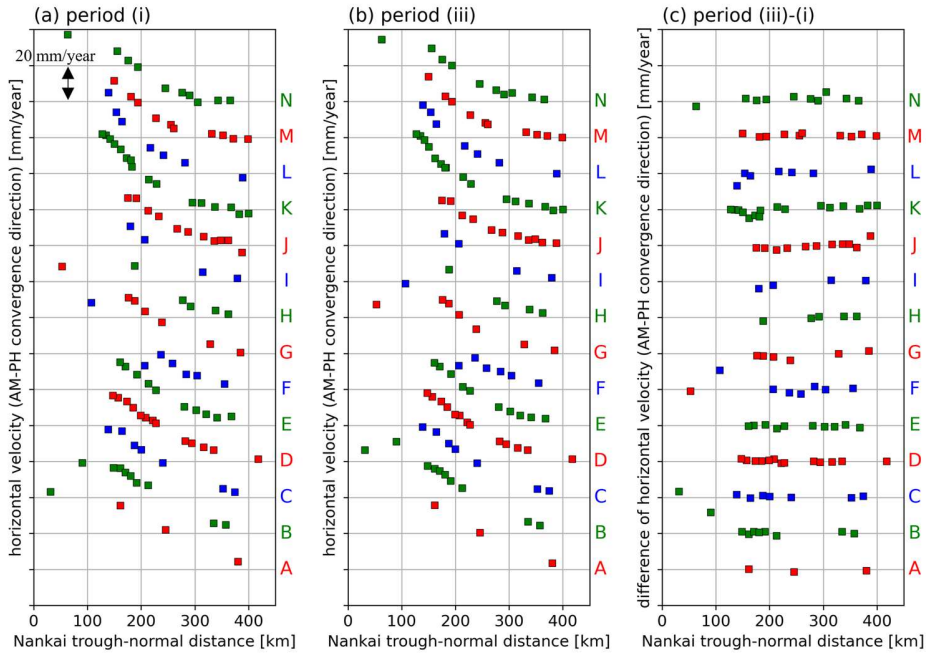


Figure S3. Profiles of GNSS horizontal velocities in the AM-PH convergence direction. The locations of the profile lines (A–N) are shown in Figure 2. (a), (b), and (c) correspond to profiles indicated in Figure 2a, b, and c, respectively.

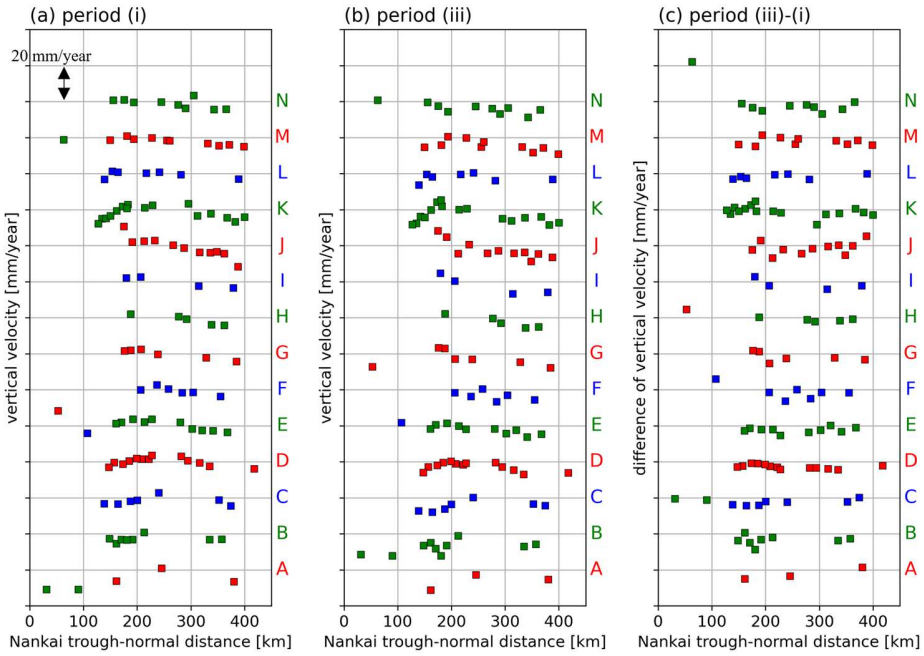


Figure S4. Same as Figure S3 but for GNSS vertical displacement velocities.

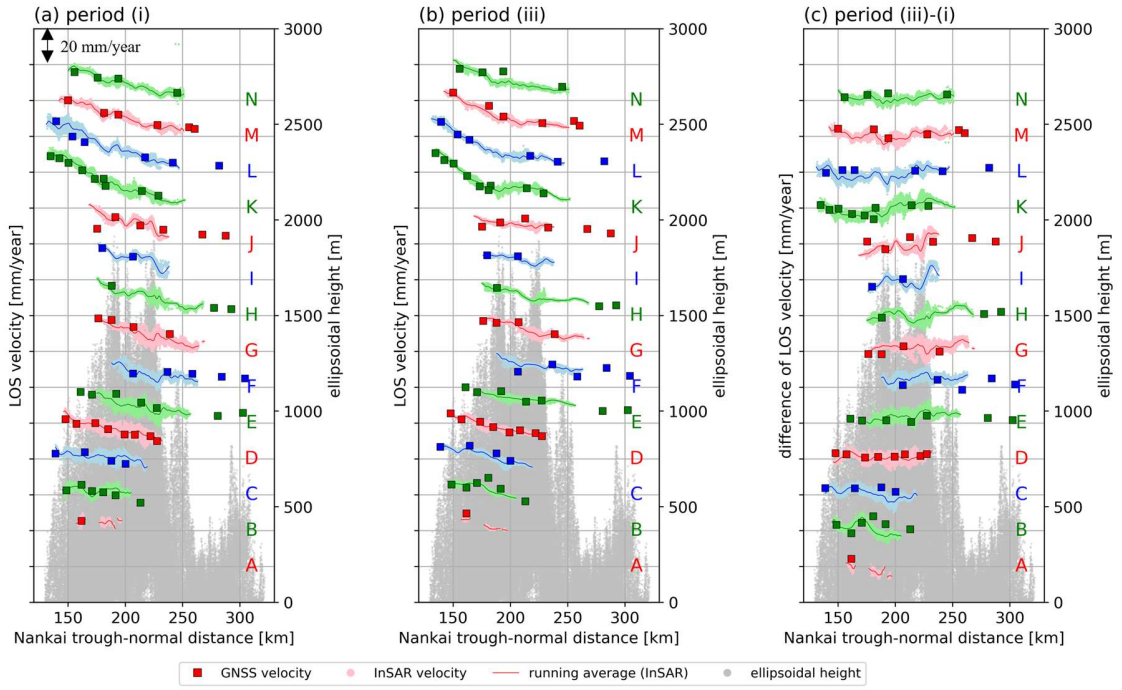


Figure S5. Profiles of LOS velocities for descending frames. We plot InSAR velocities as dots, their running averages as colored solid lines, and GNSS velocities projected into the LOS directions as squares. We also plot ellipsoidal heights as gray dots. (a), (b), and (c) correspond to profiles indicated in Figure 2d, e, and f, respectively.

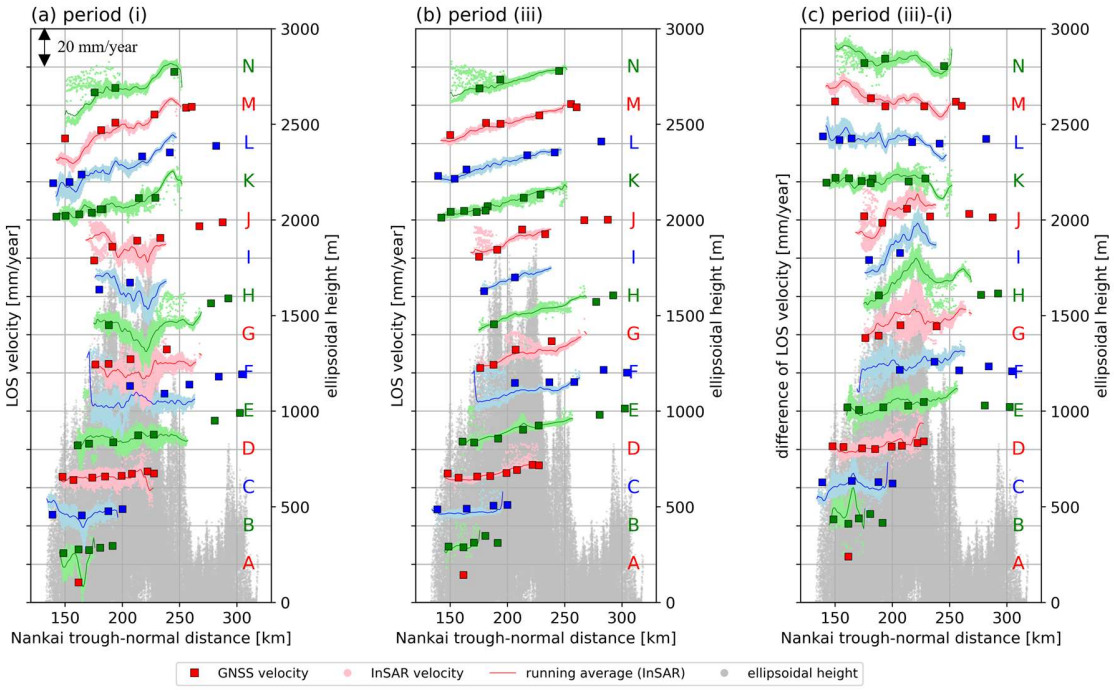


Figure S6. Same as Figure S5 but for LOS velocities in ascending frames.

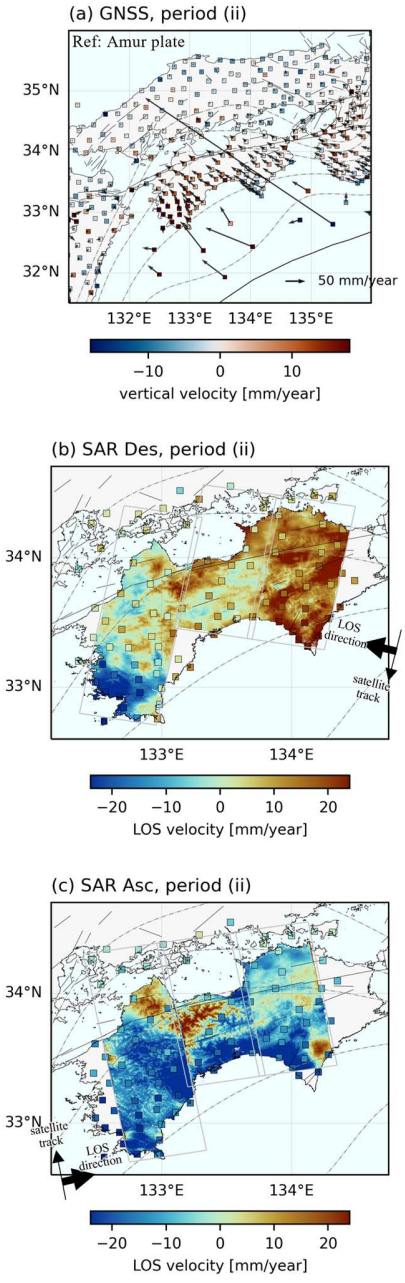


Figure S7. Observed velocity fields in period (ii).

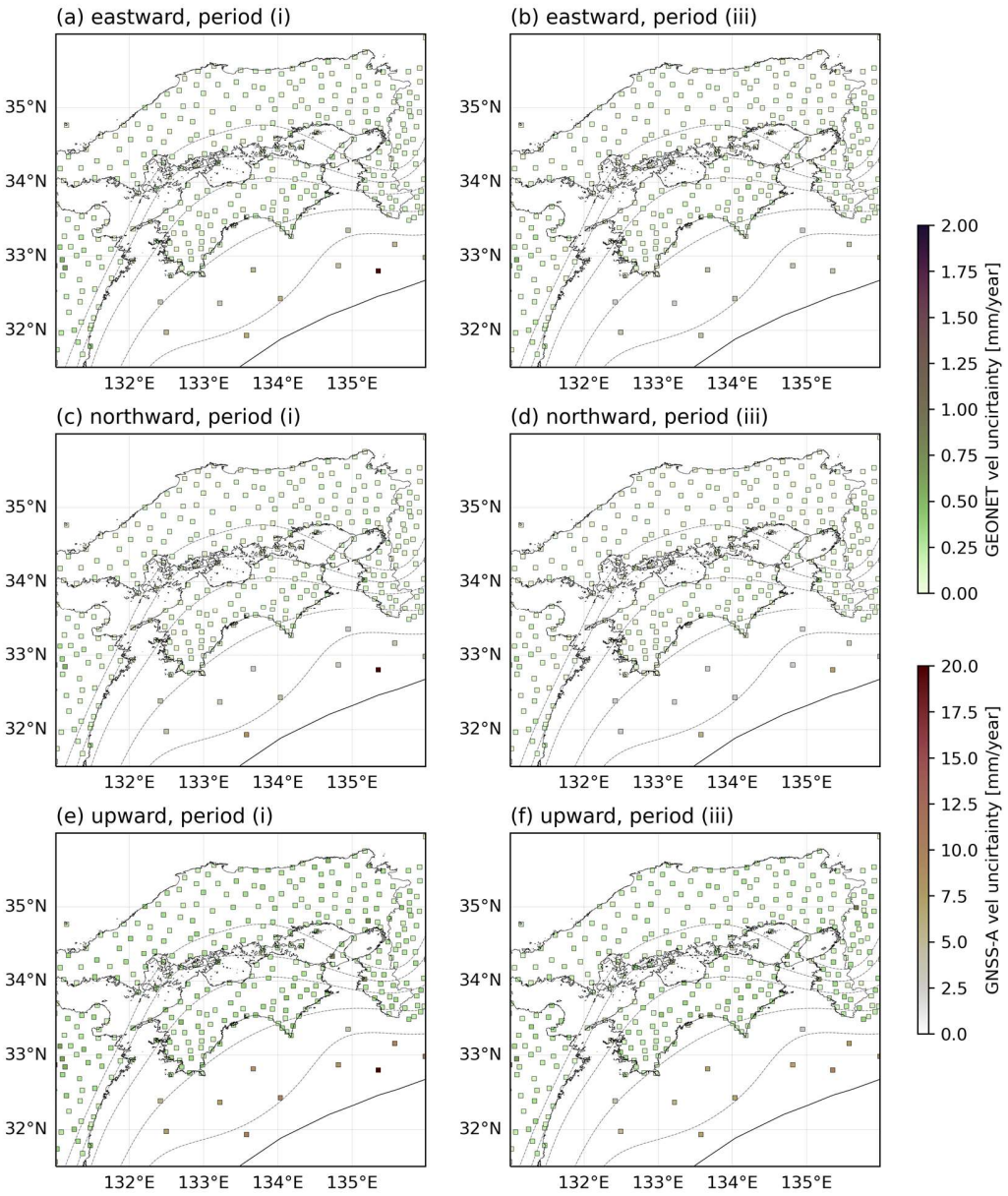


Figure S8. Standard errors of the estimated GNSS velocities obtained during the function fitting in the GNSS processing.

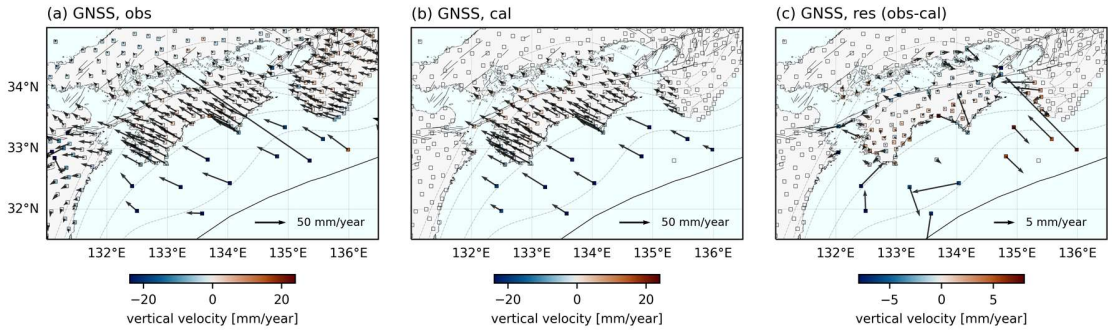


Figure S9. Same as Figure 4 but for the GNSS model.

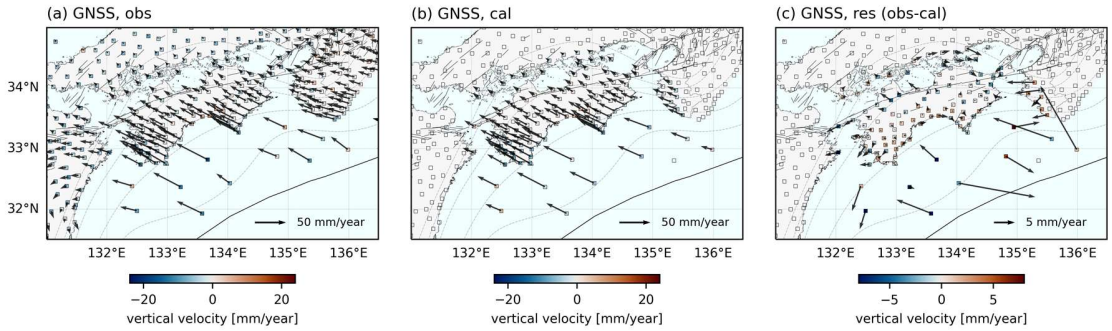


Figure S10. Same as Figure 5 but for the GNSS model.

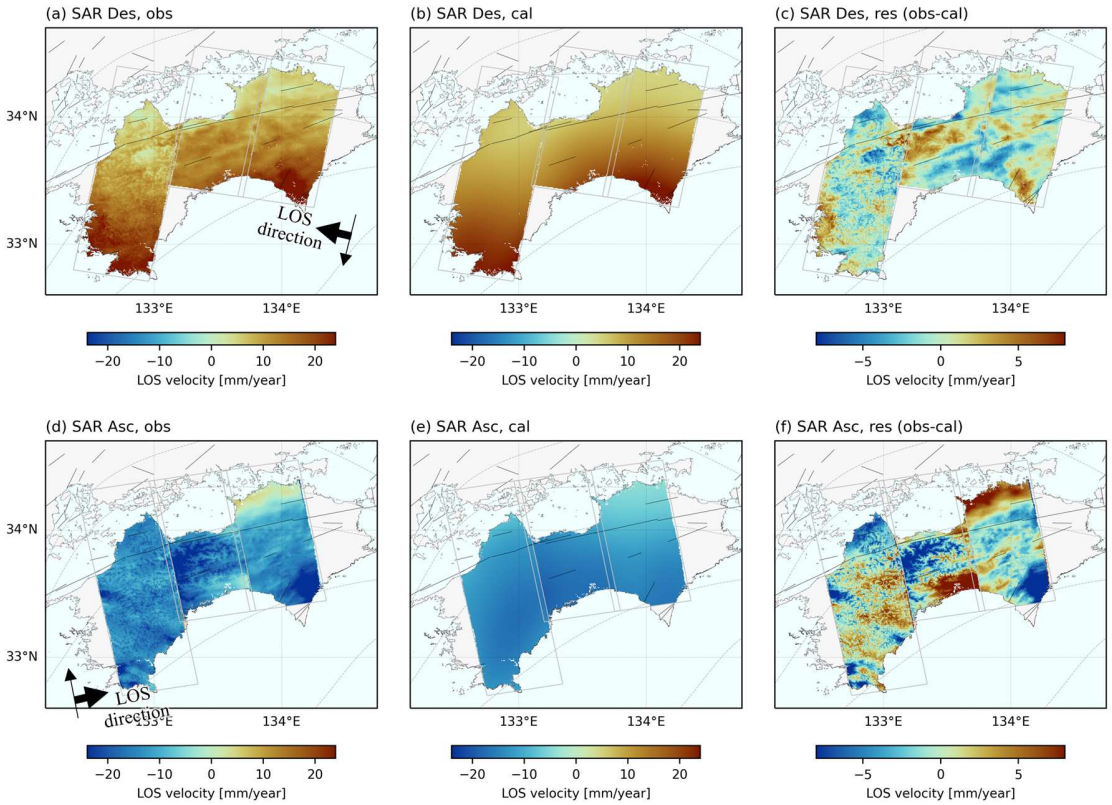


Figure S11. Same as Figure 4 but for the InSAR model.

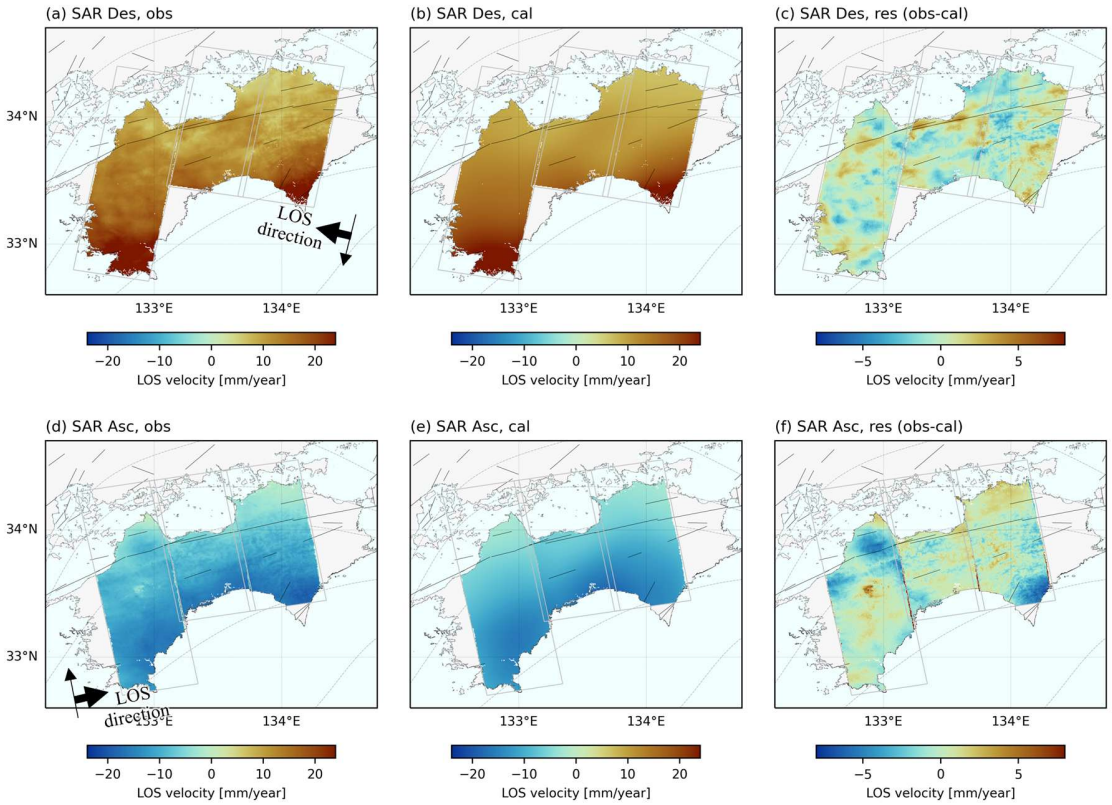


Figure S12. Same as Figure 5 but for the InSAR model.

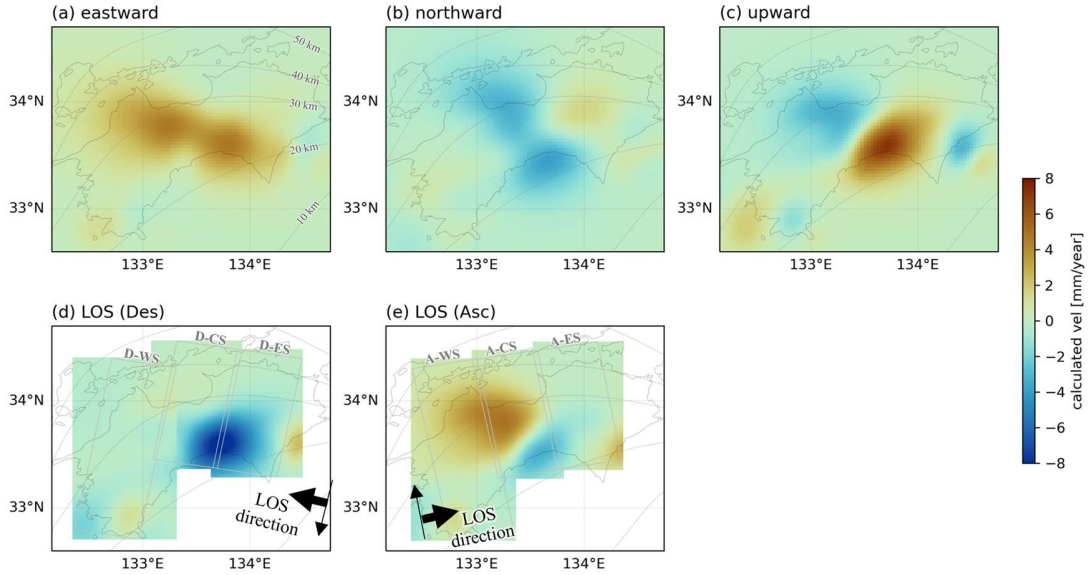


Figure S13. Theoretical velocity changes calculated from estimated slip deficit rate change in the joint model between periods (i) and (iii) (shown in Figure 3i).

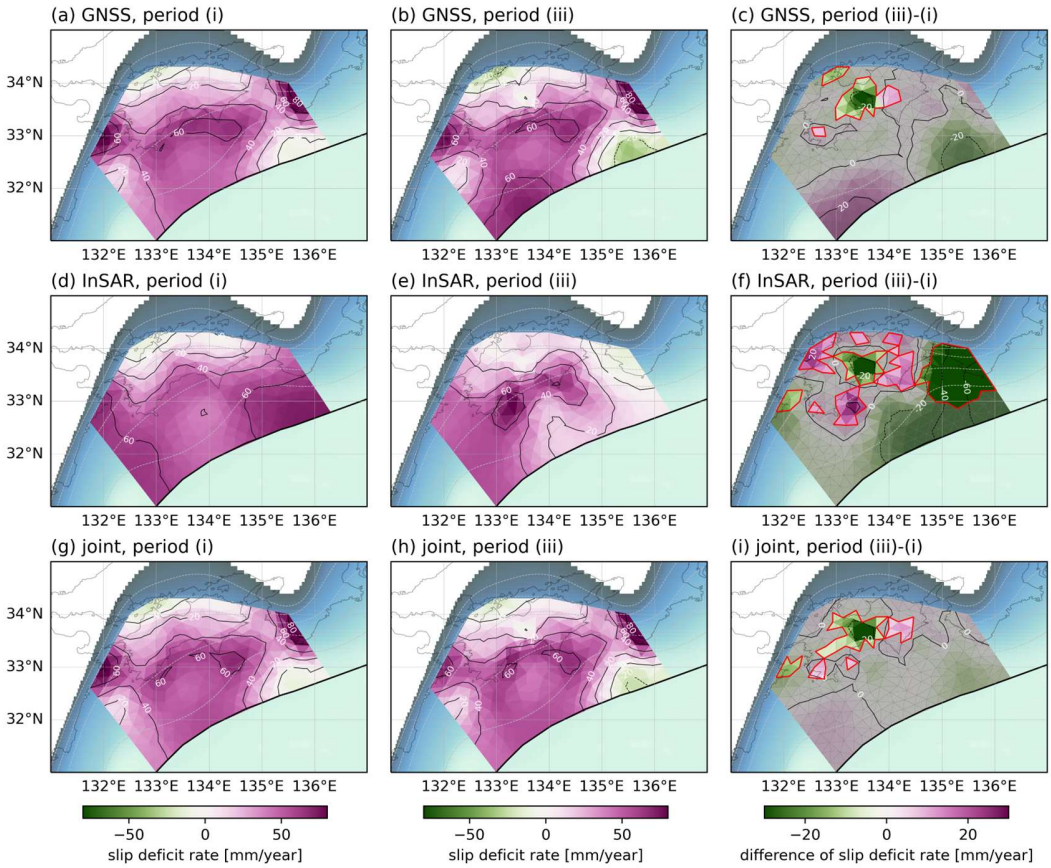


Figure S14. Same as Figure 3 but for slip deficit rate distributions estimated with a free-slip boundary condition.

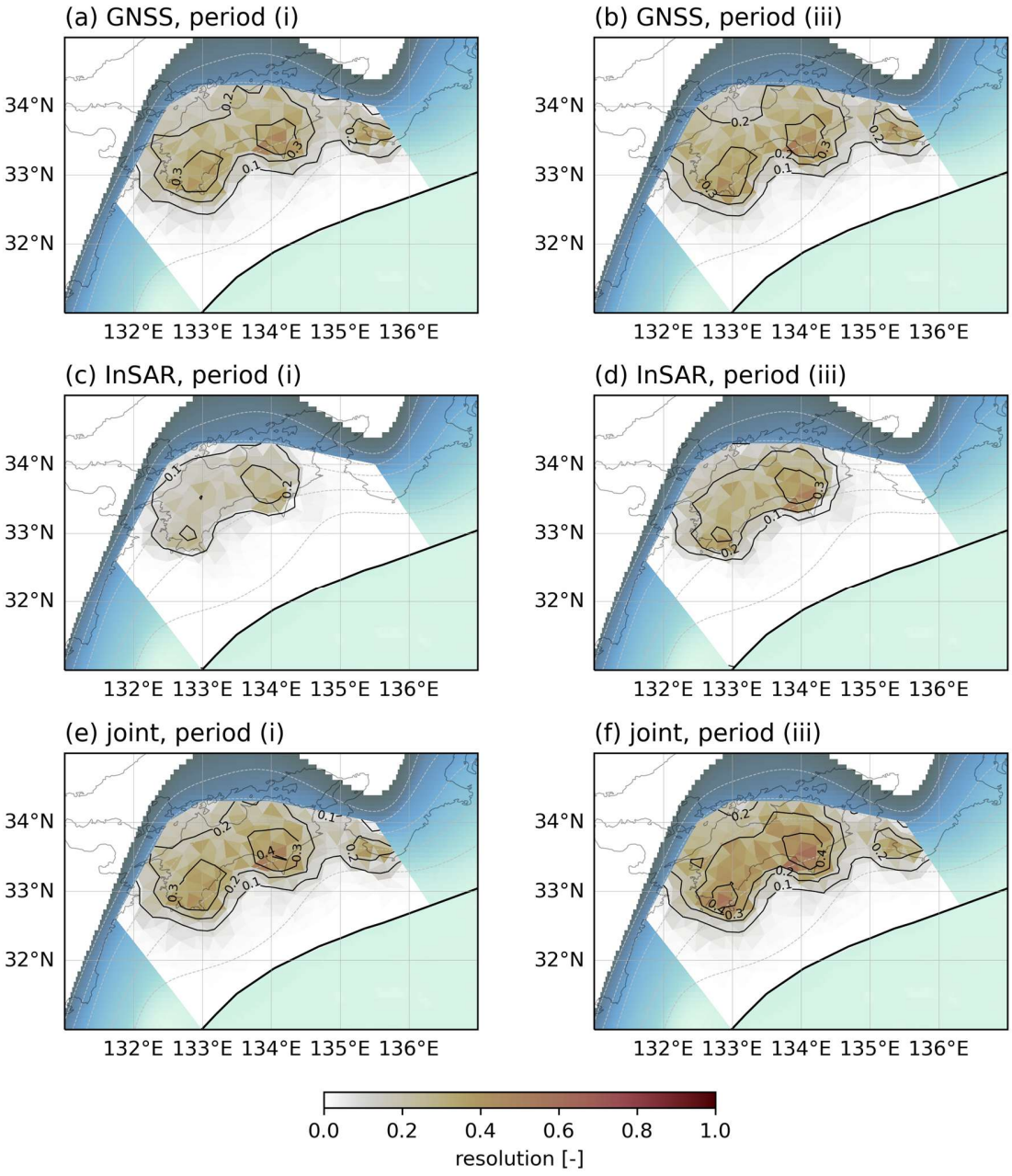


Figure S15. Diagonal components of $\boldsymbol{R_m}$ defined in equation (S23).

Table S1. Information on the ALOS-2 SAR data used in this study.

	Path-frame	Off-nadir angle (beam No.)	Analysis period	Number of SAR images
Descending, West Shikoku	22-2930, 2940, 2950	32.4° (U2-7)	3 September 2014 to 19 February 2025	35
Descending, Central Shikoku	21-2930, 2940	38.2° (U2-9)	10 October 2014 to 28 March 2025	29
Descending, East Shikoku	21-2930, 2940	35.4° (U2-8)	26 September 2014 to 5 July 2024	37
Ascending, West Shikoku	129-650, 660, 670	32.4° (U2-7)	23 August 2014 to 8 February 2025	24
Ascending, Central Shikoku	129-660, 670	35.4° (U2-8)	20 September 2014 to 22 February 2025	24
Ascending, East Shikoku	129-660, 670	38.2° (U2-9)	4 October 2014 to 8 March 2025	23

Table S2. Root mean square error (RMSE) values between InSAR and GNSS velocities in LOS directions.

	Period (i)	Period (ii)	Period (iii)
Descending West Shikoku	2.94 mm/yr	8.70 mm/yr	2.06 mm/yr
Descending Central Shikoku	3.34 mm/yr	6.87 mm/yr	1.73 mm/yr
Descending East Shikoku	3.60 mm/yr	8.73 mm/yr	1.97 mm/yr
Ascending West Shikoku	4.16 mm/yr	11.4 mm/yr	2.45 mm/yr
Ascending Central Shikoku	7.07 mm/yr	12.6 mm/yr	1.64 mm/yr
Ascending East Shikoku	4.59 mm/yr	12.6 mm/yr	1.50 mm/yr